LETTER

Sliceable, Moldable, and Highly Conductive Electrolytes for All-Solid-State Batteries

Tej P. Poudel, Erica Truong, Ifeoluwa P. Oyekunle, Michael J. Deck, Bright Ogbolu, Yudan Chen, Pawan K. Ojha, Thilina N. D. D. Gamaralalage, Sawankumar V. Patel, Yongkang Jin, Dewen Hou,* Chen Huang, Tianyi Li, Yuzi Liu, Hui Xiong, and Yan-Yan Hu*

Read Online

ACCESS | Metrics & More | Article Recommendations | Supporting Information

ABSTRACT: All-solid-state batteries (ASSBs) require solid electrolytes with high ionic conductivity, stability, and deformability for optimal energy and power density. We developed lithium-deficient lithium yttrium bromide (LYB) solid electrolytes, $Li_{3-x}YBr_{6-x}$ ($0 \leq x \leq 0.50$), using a comelting method with controlled lithium deficiency. These electrolytes exhibit favorable mechanical properties such as high moldability and sliceability. The $Li_{2.65}YBr_{5.65}$ composition has an ionic conductivity of 4.49 mS cm^{-1} at 25 °C and an activation energy of 0.28 eV. Compared to Li_3YBr_6, $Li_{2.65}YBr_{5.65}$ demonstrates improved rate performance and cycling stability in ASSBs. High-resolution X-ray diffraction confirms the formation of the LYB

phase with a **C2/m** space group. Structural analysis reveals increased cation disorder and larger polyhedral volumes for $x > 0$ in $Li_{3-x}YBr_{6-x}$, contributing to reduced Li$^+$ migration energy barriers. Bond valence site energy calculations and molecular dynamics simulations reveal enhanced 3D lithium-ion transport. NMR spectroscopy further highlights increased Li$^+$ dynamics and impurity elimination.
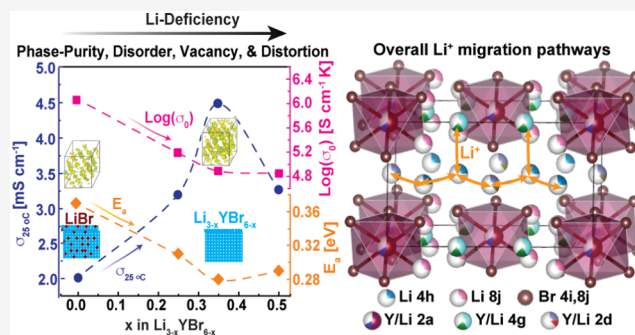
A ll-solid-state batteries (ASSBs) using solid electrolytes (SEs) offer a promising alternative to conventional lithium-ion batteries (LIBs) because they are non-flammable and can operate over a wide temperature range. Among all the inorganic SEs, halide-based SEs offer a wider electrochemical stability window and compatibility with active-cathode materials while having comparable ionic conductivity with sulfide-based SEs.[1,2] In addition to high conductivity, favorable mechanical properties are critical for the SEs. Deformability is especially important, as it enables SEs to be used effectively as thin separator sheets in batteries for increased energy densities. The polarizability and soft nature of bromides can lower the activation energy for ion transport.[3−7]

Herein, we have chosen lithium yttrium bromide (LYB) with compositions $Li_{3-x}YBr_{6-x}$ (x = 0 to 0.5) as the model system due to the high ionic conductivity via 3-D conduction pathways and the stability of the YBr_6^{3-} octahedron.[8] We have obtained highly moldable and sliceable $Li_{3-x}YBr_{6-x}$ with an ionic conductivity of 4.49 mS cm^{-1}, demonstrating a good rate and long-term cycling performance when used in ASSBs. We leverage a combination of solid-state NMR, synchrotron XRD, and electrochemical impedance spectroscopy (EIS) to characterize Li$^+$ dynamics and short- and long-range structures. The ab initio molecular dynamics (AIMD) simulation and

bond valence site energy (BVSE) calculation support the overall increase in conductivity with Li-deficiency featuring a more dispersed 3D network and decreased migration barrier with increased bottleneck size.

The comelting synthesis of $Li_{3-x}YBr_{6-x}$ followed by controlled slow cooling yielded highly crystalline structures, evident in the obtained transparent crystalline chunk (Figure 1). All of the samples possess remarkable softness, allowing for deformability (Figure 1a). Their pliable nature can benefit conformal contact with electrodes at the interfaces, improving the mechanical stability of devices and enhancing ion transport efficiency in ASSBs. The sliceability and moldability of these materials make it easier to fabricate ASSBs. A thin pellet of $Li_{3-x}YBr_{6-x}$ can be prepared by slicing (Figure 1a) or cold pressing the co-melted samples, which can significantly
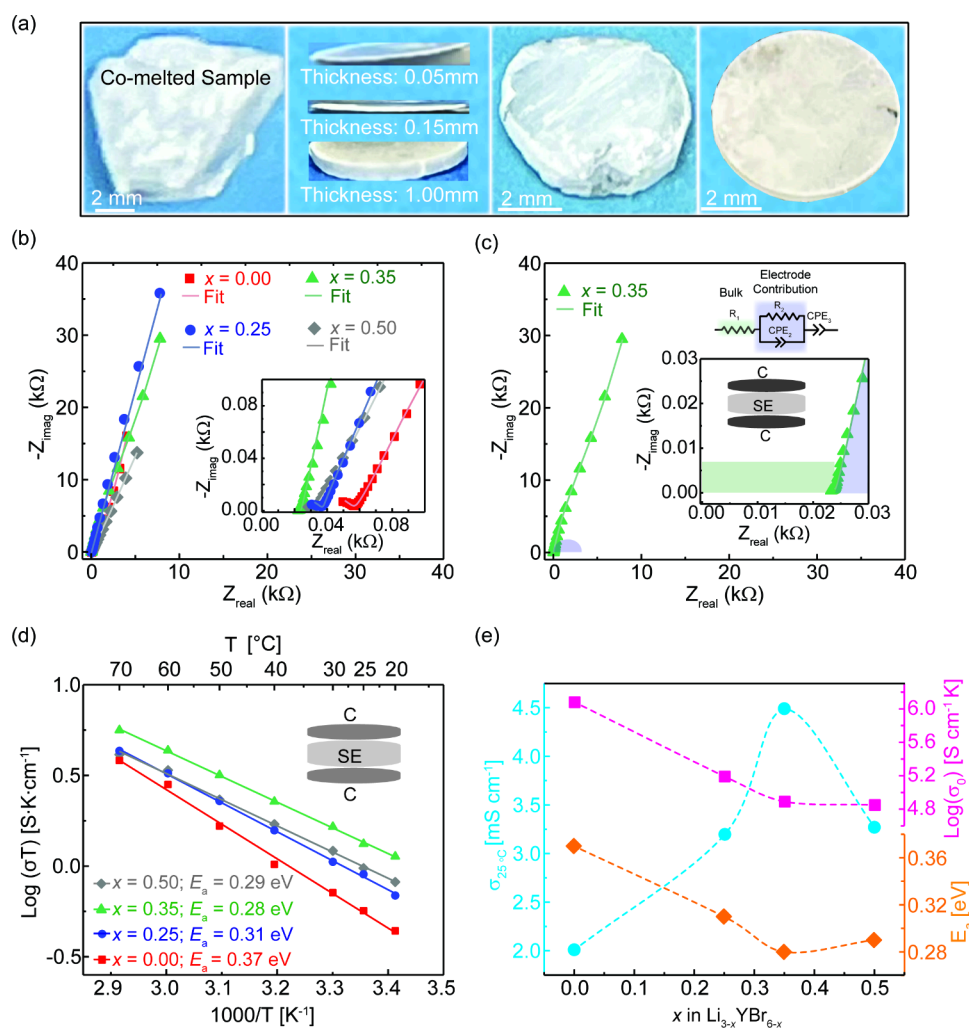
Figure 1. (a) Picture of an as-synthesized soft piece of $Li_{2.65}YBr_{5.65}$ crystal (left), followed by the pictures of slices taken from the $Li_{3-x}YBr_{6-x}$ crystal with different thicknesses using a manual blade (middle two, from top and side angles of view, respectively, the 1-mm-thick pellet from the cold press is used as a reference), demonstrating the sliceability of the crystal, desirable for preparing thin SEs, and picture of a gently cold-pressed pellet using the as-synthesized crystal, illustrating the moldability of $Li_{3-x}YBr_{6-x}$ crystals (right). (b) Overlay of the Nyquist plots of $Li_{3-x}YBr_{6-x}$ ($x = 0, 0.25, 0.35,$ and 0.5) at 25 °C. (c) Representative Nyquist plot for $Li_{3-x}YBr_{6-x}$ ($x = 0.35$) at 25 °C and equivalent circuit fitting. The mid-frequency semicircle is assigned to the electrode contribution with a capacitance of $\sim$7.23 μF.[12,13] (d) Arrhenius plot and activation energy of the prepared $Li_{3-x}YBr_{6-x}$. (e) Ionic conductivity at 25 °C, activation energy, and Arrhenius prefactor, each as a function of x in $Li_{3-x}YBr_{6-x}$.

improve the energy densities of ASSBs when used as a thin separator in ASSBs.

Fast-ion transport is critical to materials used as SEs in ASSBs. The ion transport properties of $Li_{3-x}YBr_{6-x}$ were evaluated by using AC impedance spectroscopy. Figure 1b shows the Nyquist plots of $Li_{3-x}YBr_{6-x}$ at 25 °C measured using a C|SE|C setup. From the magnified view shown in the inset of Figure 1b, we observe a decrease in impedance with lithium deficiency up to $x = 0.35$, and the impedance increases for further Li-deficiency. Representative Nyquist plot fitting using the equivalent circuit model of the highest conductive SE is presented in Figure 1c, with the rest of the series presented in Figure S1 and fitting parameters listed in Table S1. The high-frequency semicircle is attributed to the ion transport process in the bulk of the solid electrolyte,[9−11] and the middle-frequency semicircle is to the electrode contribution with a typical capacitance of 7.23 μF for the most conductive sample.[12,13] The resistance extracted from the bulk impedance is used to calculate conductivity by using the following

equation: $\sigma_{DC} = \frac{L}{R \times A}$, where L and A are the thickness of the pellet and surface area of the blocking electrode, respectively, and R is the value of resistance extracted from the equivalent circuit fitting. The overall conductivity increases from 2.02 mS cm^{-1} for $x = 0.00$ to 4.49 mS cm^{-1} for $x = 0.35$ in $Li_{3-x}YBr_{6-x}$, indicating that the Li deficiency promotes ion transport. A slight decrease in conductivity was obtained with increasing Li-deficiency beyond $x = 0.35$.

Variable-temperature EIS (VT-EIS) was performed, and the exemplary Nyquist plots for $x = 0.35$ are presented in Figure S2. The conductivity was calculated for the measured temperature range (20−70 °C) utilizing the resistance extracted from the equivalent circuit fitting of the Nyquist plots. An Arrhenius behavior was observed for all of the $Li_{3-x}YBr_{6-x}$ samples. The activation energy of prepared $Li_{3-x}YBr_{6-x}$ was calculated using the slope of the Arrhenius-type plot and is shown for the corresponding compositions in Figure 1d. The ionic conductivity at 25 °C, activation energy, and Arrhenius-type prefactor as functions of x in $Li_{3-x}YBr_{6-x}$
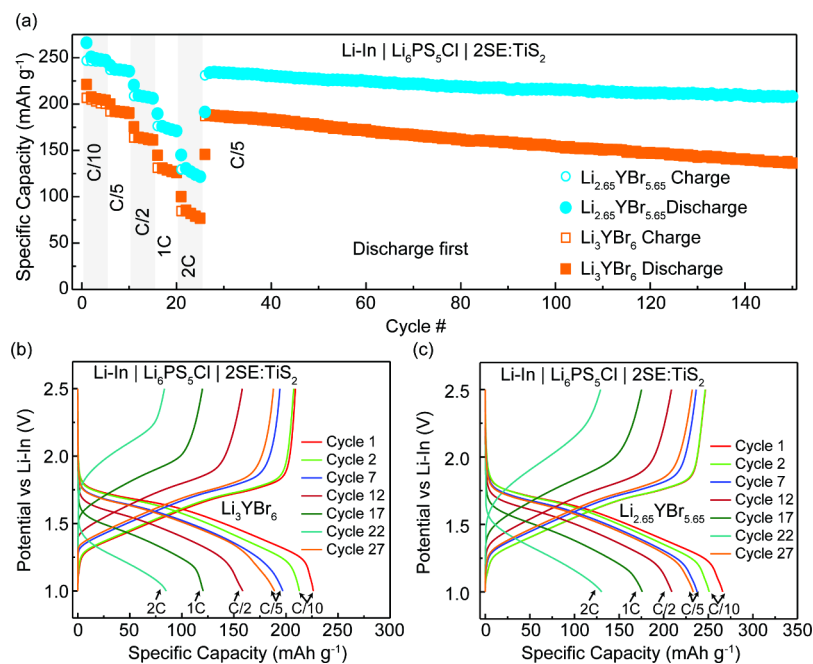
Figure 2. Galvanostatic cycling of the LYB-TiS$_2$ catholyte with Li$_6$PS$_5$Cl as the separator. (a) Rate performance of the Li−In|LPSCl|2SE:TiS$_2$ cell (SE = Li$_3$YBr$_6$ or Li$_{2.65}$YBr$_{5.65}$) followed by long-term cycling at C/5. Voltage profile of Cycle 1 along with the 2nd cycles of each C-rate for (b) the Li−In|LPSCl|2(Li$_3$YBr$_6$):TiS$_2$ cell and (c) the Li−In|LPSCl|2(Li$_{2.65}$YBr$_{5.65}$):TiS$_2$ cell.

are shown in Figure 1e and listed in Table S2. The linearity of the Arrhenius-type plots indicates no major phase change or degradation within the examined range of temperature. The activation energy for $x = 0.00$ is 0.37 eV, $x = 0.25$ is 0.31 eV, $x = 0.35$ is 0.28 eV, and $x = 0.50$ is 0.29 eV. The decrease in activation energy with Li-deficiency correlates with increased conductivity at room temperature. The Arrhenius prefactor decreases with increased Li deficiency.

To confirm that the measured conductivities are from ion migration, the electronic conductivity of Li$_{2.65}$YBr$_{5.65}$ was determined using the DC polarization method. The DC polarization plots measured at four different voltages (100, 200, 300, and 400 mV) are shown in Figure S3. The electronic contribution for Li$_{2.65}$YBr$_{5.65}$ is 5.92×10^{-9} S cm^{-1}. This low electronic conductivity confirms that the total conductivity, 4.49 mS cm^{-1}, is largely from ionic transport. The detailed electrochemical window characterization and carbon-composite cell cycling are presented in the Supporting Information (SI, Figures S4−S7).

To test the performance of Li$_{3-x}$YBr$_{6-x}$ in batteries, ASSB half-cells were fabricated with the setup of Li−In|Li$_6$PS$_5$Cl| 2(Li$_3$YBr$_6$):TiS$_2$ and Li−In|Li$_6$PS$_5$Cl|2(Li$_{2.65}$YBr$_{5.65}$):TiS$_2$, where TiS$_2$ was used as cathode active material (CAM). A comparison of Nyquist plots of the half-cells at 25 °C along with the fitted equivalent circuit model is shown in Figure S8. The bulk resistance of the separator, the CAM/LYB resistance in the catholyte, the separator-catholyte interfacial resistance (Separator|Catholyte), and the interfacial resistance between bulk and Li−In alloy (Separator|Li−In) were extracted and presented in Table S3 and explained in detail in SI. The CAM/ LYB resistance is significantly lower (2.49 Ω) for the 2Li$_{2.65}$YBr$_{5.65}$:TiS$_2$ containing cell compared with the 2Li$_3$YBr$_6$:TiS$_2$ containing cell (23.9 Ω). This may be attributed to the higher ionic conductivity, improved softness, and elimination of the LiBr impurity phase in Li$_{2.65}$YBr$_{5.65}$ compared with Li$_3$YBr$_6$. The assembled half-cells were

evaluated for their performance across a range of C-rates using galvanostatic cycling at 22 °C in the 1−2.5 V voltage range vs Li/In. The theoretical capacity of 239 mAh g^{-1} for TiS$_2$ was used to calculate the C-rates (charge−discharge). The cells were cycled for 5 cycles at each C-rate, followed by 125 cycles at 0.2 C. Figure 2a displays the specific capacity versus cycle number for the half-cells, and the corresponding voltage profiles for the selected cycles are presented in Figures 2b and 2c. In contrast, the Li$_{2.65}$YBr$_{5.65}$-containing cell exhibited a higher initial discharge capacity, reaching 266 mAh g^{-1} (Figures 2a and 2c). Similarly, its initial charge capacity of 247 mAh g^{-1} surpassed that of the Li$_3$YBr$_6$ cell (208 mAh g^{-1}). This trend continues in the second cycle, with the Li$_{2.65}$YBr$_{5.65}$-containing cell maintaining a slightly higher discharge capacity (250 mAh g^{-1}) and stable charge capacity (247 mAh g^{-1}) (Figures 2a−c). Both cells demonstrated remarkable rate capabilities, delivering 85 mAh g^{-1} and 130 mAh g^{-1} at the high rate of 2 C for the Li$_3$YBr$_6$- and Li$_{2.65}$YBr$_{5.65}$-containing cells, respectively. Notably, upon returning to 0.2 C after 26 cycles, both cells retained high stability during extended cycling for 125 cycles. Additionally, both cells showcased high Coulombic efficiency of more than 99% throughout the extended cycling, as shown in Figure S9a. The capacity retention from the 27th cycle to the 150th cycle is ∼89% for the Li$_{2.65}$YBr$_{5.65}$-containing cell, while the Li$_3$YBr$_6$-containing cell degrades slightly faster than that. As shown in Figures S9b and S9c, both cells exhibit characteristic redox peaks associated with the Ti^{3+}/Ti^{4+}.[14,15] The slightly higher capacity observed for the Li$_{2.65}$YBr$_{5.65}$-containing cell could be due to the better interfacial contact, reversible capacity generation from SE (Figure S5), and the small peak observed at ∼1.2 V vs. Li−In (Figure S9c) from an unknown redox reaction. The overpotential increases with the increasing C-rate. The overall enhanced performance for the Li−In| Li$_6$PS$_5$Cl|2Li$_{2.65}$YBr$_{5.65}$:TiS$_2$ cell can be attributed to the combined effect of enhanced ionic conductivity, improved
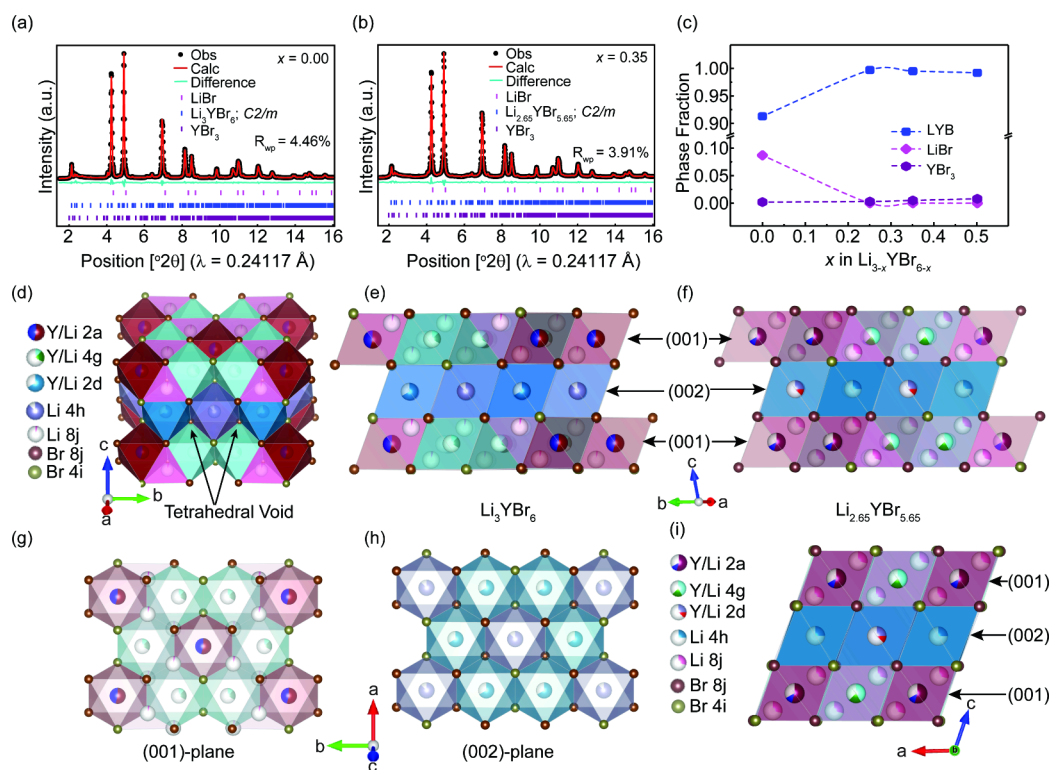
Figure 3. High-resolution X-ray diffraction patterns and refinement for $Li_{3-x}YBr_{6-x}$: (a) $x = 0$ and (b) $x = 0.35$. (c) Phase quantification as a function of x in $Li_{3-x}YBr_{6-x}$. LiBr impurity is minimized in the Li-deficient compositions. (d) Monoclinic crystal structure (space group: $C2/m$) of $Li_{3-x}YBr_{6-x}$. All the octahedra are edge-connected, revealing the honeycomb-like pattern along the c and b directions. Staggered stacking of the (001) and (002) lattice planes of (e) Li_3YBr_6 and (f) $Li_{2.65}YBr_{5.65}$. In the crystal structure of $Li_{2.65}YBr_{5.65}$, the Li^+ occupancy in the 8j tetrahedra increases significantly compared with Li_3YBr_6. Cation ordering in the (g) (001)-plane and (h) (002)-plane. (i) $Li_{2.65}YBr_{5.65}$ structure viewed from the b-direction. The structure shows the low occupancy of cations in the (002) plane.

utilization of CAM,[16] and elimination of poor conducting LiBr (Figure S10) impurity.

Understanding the phase purity and structure of $Li_{3-x}YBr_{6-x}$ is crucial for deciphering structure-ion transport correlations. Therefore, detailed lab powder X-ray diffraction (XRD) analysis was conducted on the prepared SEs, and the results are discussed in the SI (Figures S11 and S12). To accurately determine the bulk structural parameters such as atomic coordinates, site occupancies, and thermal parameters of $Li_{3-x}YBr_{6-x}$, further structural investigation was conducted using high-resolution XRD, and the diffractograms are shown in Figure S13a, which can be indexed to a monoclinic structure with the $C2/m$ space group. The inset of Figure S13b illustrates the emergence of triangular Warren-type peak shapes within the 2θ range of $2°-3°$; this observation signifies the existence of planar defects and dislocations, commonly referred to as stacking faults.[17−19] High-resolution XRD confirms the existence of the LiBr impurity phase for $x = 0.00$ in , however, for $x \geq 0.25$, the LiBr impurity is eliminated. Furthermore, a trace amount of unreacted YBr_3 precursor was also detected, as evident from the magnified view of the high-resolution XRD patterns shown in Figure S13b.

Rietveld refinement was used to analyze and quantify the effects of lithium deficiency on lithium site occupancy, impurity phases, cation site disorder, polyhedron distortion, and polyhedral volume. Figures 3a, 3b, and S14 present the refined powder diffraction patterns. The refinement results are plotted and displayed in Figures 3, S15, and S16 with the lattice and atomic parameters listed in Tables S4−S7. The phase fraction refinement was performed to determine the

phase purity of $Li_{3-x}YBr_{6-x}$, which reveals that the LiBr impurity phase is significantly reduced in $Li_{3-x}YBr_{6-x}$ with $x > 0$ (Figure 3c). These results show that Li deficiency in Li_3YBr_6 can eliminate the LiBr impurity, which was observed in significant amounts (3−8 wt %) in previous studies on Li_3YBr_6.[1,12,20]

Rietveld refinement against high-resolution XRD data confirmed the monoclinic ccp anion framework with the $C2/m$ space group of LYB, consistent with previous reports.[21] As depicted in Figure 3 and Table S4, the LYB structure features two distinct Br^- sites (4i and 8j Wyckoff positions) and five cation sites (2a, 2d, 4g, 4h, and 8j Wyckoff positions) occupied by either Y^{3+}, Li^+, or mixed. The (001)-plane (Figure 3g) reveals a honeycomb-like structure formed by edge-sharing 2a and 4g octahedra, which are face-shared with 8j tetrahedra. The (002)-plane (Figure 3h), contains edge-shared 4h and 2d octahedra, forming a honeycomb-like structure. Notably, this (002)-layer comprises only $LiBr_6^{5-}$ octahedra, face-shared with interstitial tetrahedral voids. The 3D views of the (001) and (002) layers are given in Figure S15. The tetrahedral voids shown in Figure 3d serve as lithium migration channels within the $C2/m$ structure, enabling efficient Li^+ conduction.[1,12]

Detailed analysis unveils specific site occupancy patterns within the LYB (Figures 3 and S16). In the stoichiometric Li_3YBr_6, within the 001 planes, 2a Wyckoff sites are fully occupied with ∼60% Y^{3+} and 40% Li^+. In contrast, 4g Wyckoff sites are largely vacant, with approximately 20% occupied by Y^{3+} cations and 10% occupied by Li^+. The 2d and 4h Wyckoff sites in the 002-planes are occupied by only Li^+. The interstitial 8j sites are mostly vacant, with <5% occupied by Li^+.
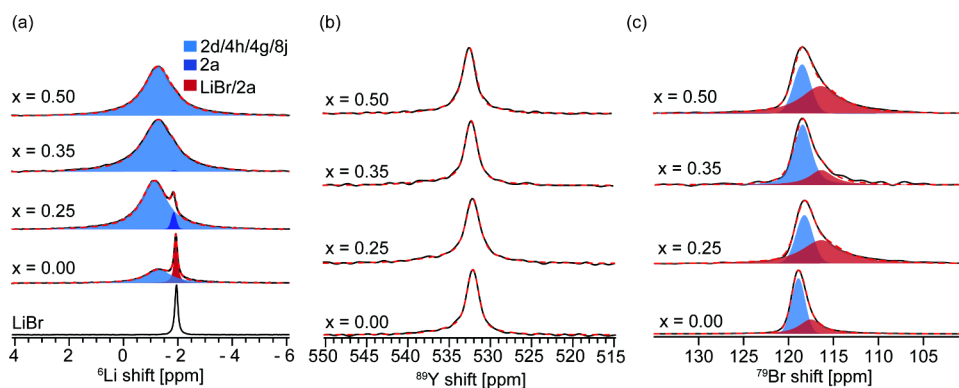
Figure 4. Characterization of $Li_{3-x}YBr_{6-x}$ ($x = 0$, 0.25, 0.35, and 0.5) using ^6Li, ^{89}Y, and ^{79}Br MAS NMR. (a) ^6Li NMR spectra with resonance assignments. The LiBr impurity is minimized from the sample when $x \neq 0$. (b) ^{89}Y NMR spectra with corresponding spectral fits for resonances associated with Li_3YBr_6 and (c) ^{79}Br NMR spectra of $Li_{3-x}YBr_{6-x}$ and corresponding spectral fits.
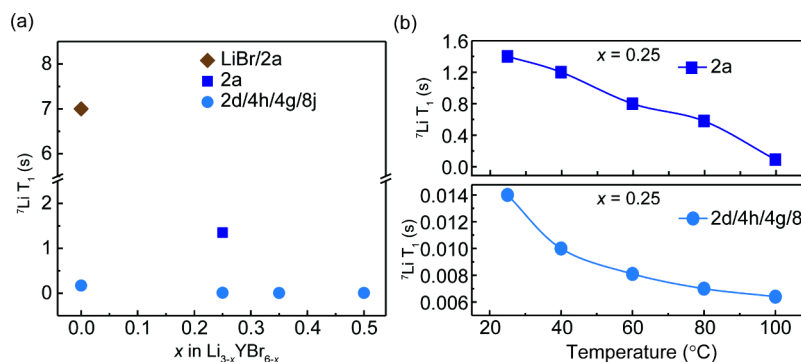
Figure 5. ^7Li T_1 NMR relaxation time measurements to probe Li^+ dynamics: (a) ^7Li T_1 relaxation times. (b) Variable-temperature ^7Li NMR T_1 for $x = 0.25$ in $Li_{3-x}YBr_{6-x}$.

Compared to Li_3YBr_6, the long-range structure of Li-deficient LYB ($x \geq 0.25$ in $Li_{3-x}YBr_{6-x}$) is not significantly different (Tables S5−S7). This is evident from their similar stacking patterns shown in Figures 3e and 3f for $x = 0.00$ and $x = 0.35$, respectively. With Li deficiency, the system becomes yttrium-rich, and the excess Y^{3+} substitutes Li^+, primarily occupying 2d sites within the (002) planes. Li^+ occupancy in the previously underutilized 8j-tetrahedral sites increases significantly with Li deficiency in LYB (Figure 4), and Li^+ vacancies are created at 4h sites for $x > 0.25$ in $Li_{3-x}YBr_{6-x}$. Overall, by introducing Li deficiency in $Li_{3-x}YBr_{6-x}$, Y^{3+} ions are added, and Li^+ ions are removed from the (002) planes; net Li^+ ions migrate to the interstitial 8j sites. Within the (001) planes, Y^{3+} occupancies at sites 2a and 4g remain unaltered with Li deficiency, but Li^+ redistribution occurs. The effect of x in $Li_{3-x}YBr_{6-x}$ in lattice parameters, polyhedral volume, and cation site ordering is discussed in detail in the SI (Figure S16). The morphological characterization of the highest conductive sample is also discussed in the SI (Figure S17).

Local structural characterization was carried out by using solid-state magic-angle-spinning (MAS) NMR spectroscopy. The ^6Li MAS NMR (Figure 4a) reveals that with increasing deficiency, the sharp component resonating at approximately −1.9 ppm, attributed partly to LiBr(s), significantly decreases and becomes unobservable in $Li_{3-x}YBr_{6-x}$ for $x = 0.35$ and 0.5. ^6Li NMR of LiBr(s) was acquired to support the assignment (Figure 4a). The resonance at −1.9 ppm disappears in $Li_{3-x}YBr_{6-x}$ ($x > 0$), echoing the disappearance of the LiBr impurities observed with diffraction. Instead, a new and slightly broader ^6Li resonance centered around −1.8 ppm appears in

$Li_{3-x}YBr_{6-x}$ ($x = 0.25$). This −1.8-ppm resonance has a distinct NMR relaxation behavior (see the Ion Dynamics Section, Figure 5) compared with the −1.9-ppm resonance observed in Li_3YBr_6 (Figure 4a), confirming a different origin. DFT NMR calculations were performed to assist with the NMR assignments, and the results are shown in Table 1. Two major

Table 1. ^6Li NMR Shifts, Calculated Using CASTEP

composition x in $Li_{3-x}YBr_{6-x}$	^6Li Chemical Shift [ppm]				
	Site 1	Site 2	Site 3	Site 4	Site 5
0	−1.8	−1.2	−0.6	−0.1	0.2
0.35	−1.8	−1.3	−0.2	0.2	0.6

resonance groups are observed, with Li at Wyckoff 2a sites resonating at approximately −1.8 ppm and the remaining Li sites resonating downfield with larger ppm values. Similar halide-based electrolytes typically have shown that sites at the corner or edge of the structure, such as Wyckoff 2a sites in LYB, resonate at lower ppm.[22] Therefore, the −1.8 ppm ^6Li resonance of $Li_{3-x}YBr_{6-x}$ ($x = 0.25$) is assigned to Li at 2a sites, and the broad resonance centered around −1.2 ppm is assigned to Li at the 4g, 4h, 2d, and 8j sites. Due to fast chemical exchange among Li at 4g, 4h, 2d, and 8j sites, individual resonances are not resolved on the NMR time scale.[23] In correspondence with diffraction results, a larger structural disorder is observed with Li deficiency, resulting in the observed line broadening of ^6Li resonances from ∼85 Hz ($x = 0$ and 0.25) to ∼100 Hz ($x = 0.35$ and 0.50).[24] In addition, Li vacancies created at the Wyckoff 2a sites of

$Li_{3-x}YBr_{6-x}$ $(x > 0)$ allow its possible participation in Li^+ transport. Thus, the exchange between the 2a sites and others makes this -1.8-ppm resonance less distinct and merges with the broad resonance in $Li_{3-x}YBr_{6-x}$ $(x > 0.25)$. The additional details on line widths, shifts, and ^7Li T_1 NMR relaxation times are listed in Table S8.

^{89}Y NMR was utilized to probe the Y local structures in $Li_{3-x}YBr_{6-x}$. Figure 4b exhibits one major resonance for all of the compositions. However, a noticeable peak shift is observed from 532 ppm for $x = 0$ and 0.25 to 533 ppm for $x = 0.35$ and 0.50, likely due to additional Y occupying vacant 2d sites generated by a Li deficiency. The limit of lithium deficiency without generating impurity phases is also revealed from the ^{89}Y NMR. At $x = 0.5$, a small ^{89}Y NMR peak is observed at 493 ppm, attributed to precursor YBr_3 (Figure S18). Furthermore, ^{79}Br NMR spectroscopy was acquired to examine the local structural environment around Br (Figure 4c). Two Br resonances correspond to Br at the 4i and 8j sites in LYB (Figure 3). The LiBr resonance, expected to resonate at 119.4 ppm, is not resolved from the ^{79}Br resonance of LYB.[25]

To probe Li^+ dynamics and further distinguish ^6Li NMR resonances of $Li_{3-x}YBr_{6-x}$ based on their relaxation behaviors, ^7Li NMR T_1 relaxation experiments were performed, and the T_1 values are shown in Figure 5a and Table 2. The ^7Li T_1

**Table 2. ^7Li T_1 Relaxation Time for $Li_{3-x}YBr_{6-x}$ ($x = 0$, 0.25, 0.35, and 0.5)**

composition x in $Li_{3-x}YBr_{6-x}$	^7Li T_1 [s]	
	LiBr/2a	2d/4h/4g/8j
0	7.00	0.17
0.25	1.35	0.01
0.35	N/A	0.03
0.50	N/A	0.006

relaxation time for the sharp -1.9-ppm resonance attributed mainly to the LiBr(s) impurity in Li_3YBr_6 is 7.00 s, significantly

longer than the 1.35 s for the Li_{2a} resonance of $Li_{3-x}YBr_{6-x}$ ($x = 0.25$) at -1.8 ppm; this confirms that these two Li resonances are from different origins, albeit exhibiting similar shifts. It is worth mentioning that the -1.9-ppm resonance is mostly from LiBr(s), with an unresolved small component from Li_{2a} of LYB. The broad peak displays an even smaller ^7Li T_1 relaxation time, reaching as small as 6 ms. Variable-temperature ^7Li T_1 NMR relaxation measurements show that T_1 decreases with increasing temperature (Figure 5b). This confirms Li^+ dynamics in LYB lie in the slow-motion regime, i.e., $\omega_0\tau_c \gg 1$ ($\omega_0 = 116.6$ MHz, and τ_c is the motional correlation time for Li^+, according to the Bloembergen–Purcell–Pound theory).[26] It can be inferred that a shorter relaxation time suggests faster ion motion. Therefore, based on the ^7Li T_1 NMR relaxation times, LiBr exhibits the slowest Li^+ motion, followed by Li at Wycoff 2a sites, and Li at the other sites in LYB shows the fastest Li^+ dynamics. This is expected as Li at these corner 2a sites are less mobile, while Li at the face-sharing and edge-sharing sites, 2d/4h/4g/8j, often display higher ion mobility and are responsible for superionic activities. In addition, the tracer-exchange NMR identifies the active site from which Li^+ prefers to migrate, as discussed in the SI (Figure S19).

To understand the impact of Li-deficiency in LYB on the Li^+ density distribution and diffusion, ab initio molecular dynamics (AIMD) simulations were performed on relaxed supercells (2 × 1 × 2) of Li_3YBr_6, $Li_{2.75}YBr_{5.75}$, $Li_{2.65}YBr_{5.65}$, and $Li_{2.50}YBr_{5.50}$. Mean square displacements (MSDs) of Li^+ and the distribution probability of Li^+ (Figure 6) at 900 K are calculated. The MSD plots reveal that Li^+ exhibits diffusion in all three dimensions. Notably, introducing vacancies to the Li site results in an increased MSD of Li^+, indicating an enhanced Li^+ transport. The most substantial increase in MSD for Li^+ is observed in $Li_{2.65}YBr_{5.65}$, which nearly triples, compared to the Li_3YBr_6 composition. Additionally, the Li^+ density maps (insets of Figure 6) obtained from AIMD simulations reveal a more connected Li^+ diffusion pattern when a Li^+ vacancy is introduced. Based on these simulations, the ionic conductiv-
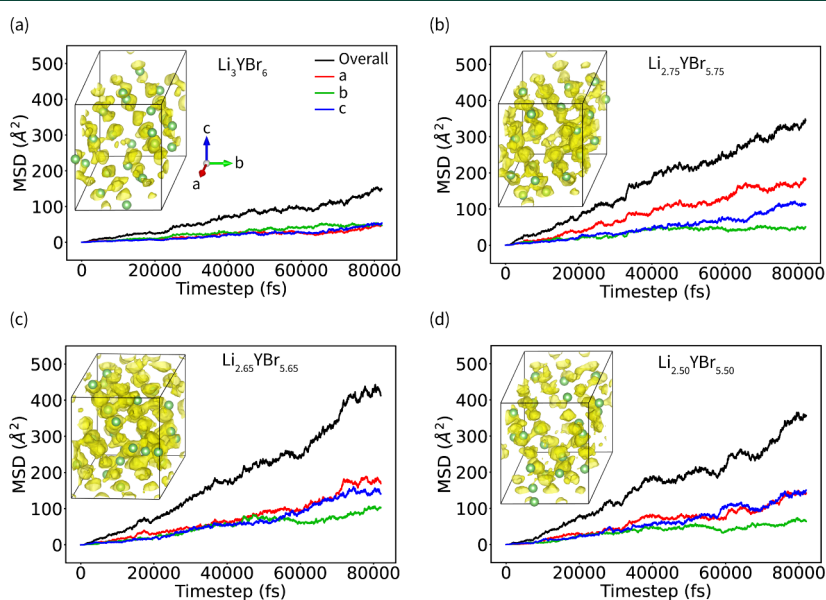
Figure 6. Mean square displacement (MSD) of Li^+ in $Li_{3-x}YBr_{6-x}$: (a) $x = 0.00$, (b) $x = 0.25$, (c) $x = 0.35$, and (d) $x = 0.50$, generated from AIMD simulations. The MSD indicates the highest Li^+ tracer diffusivity for $x = 0.35$. Corresponding Li^+ (yellow) probability density distribution in $Li_{3-x}YBr_{6-x}$ in a 2 × 1 × 2 cell based on AIMD simulations at 900 K.

ities of LYBs are predicted as follows: $Li_{2.65}YBr_{5.65}$ > $Li_{2.75}YBr_{5.75}$ ≈ $Li_{2.50}YBr_{5.50}$ > Li_3YBr_6, consistent with the experimental data. The bond valence site energy calculation is presented in the SI (Figure S20), which is also consistent with the results of the AIMD simulation.

In summary, we have synthesized a series of Li-deficient compositions, $Li_{3-x}YBr_{6-x}$ (x = 0 to 0.5), exhibiting favorable mechanical properties for preparing thin SEs in high-energy-density solid-state batteries. BVSE and AIMD simulations predict the improved Li^+ diffusion upon introducing a Li deficiency. We highlight the use of solid-state NMR, high-resolution XRD, and EIS to probe average and local structural properties and ion dynamics to deliver a comprehensive analysis on a broad time- and length-scale.[27] The improvement in ionic conductivity is correlated to the enlarged bottleneck size, decreased activation barrier, increased Li^+ dynamics, and elimination of the poor conducting impurity phase. A maximum ionic conductivity of 4.49 mS cm^{-1} at 25 °C is achieved for $Li_{2.65}YBr_{5.65}$ with an activation energy of 0.28 eV. $Li_{3-x}YBr_{6-x}$ demonstrates good rate performance and stability in ASSBs. Overall, this work paves the way for the continued exploration of Li-deficient LYB SEs and can be applied more broadly to the LMX SE family in the pursuit of high-performance energy storage devices.

■ ASSOCIATED CONTENT

Data Availability Statement

The data that supports this manuscript will be available upon request.

ⓢ Supporting Information

The Supporting Information is available free of charge at https://pubs.acs.org/doi/10.1021/acsenergylett.4c02788.

    Additional experimental details on synthesis, electrochemical characterization, electrochemical performance tests, structural characterizations, DFT NMR calculations, molecular dynamics simulations, and bond valence site energy calculation (PDF)

■ AUTHOR INFORMATION

Corresponding Authors

    Yan-Yan Hu − *Materials Science and Engineering Program, Florida State University, Tallahassee, Florida 32310, United States; Department of Chemistry and Biochemistry, Florida State University, Tallahassee, Florida 32306, United States; Center of Interdisciplinary Magnetic Resonance, National High Magnetic Field Laboratory, Tallahassee, Florida 32310, United States;* ⓞ orcid.org/0000-0003-0677-5897; Email: yhu@fsu.edu

    Dewen Hou − *Micron School of Materials Science and Engineering, Boise State University, Boise, Idaho 83725, United States;* Email: dewenhou@outlook.com

Authors

    Tej P. Poudel − *Materials Science and Engineering Program, Florida State University, Tallahassee, Florida 32310, United States*

    Erica Truong − *Department of Chemistry and Biochemistry, Florida State University, Tallahassee, Florida 32306, United States*

    Ifeoluwa P. Oyekunle − *Department of Chemistry and Biochemistry, Florida State University, Tallahassee, Florida 32306, United States*

    Michael J. Deck − *Department of Chemistry and Biochemistry, Florida State University, Tallahassee, Florida 32306, United States*

    Bright Ogbolu − *Department of Chemistry and Biochemistry, Florida State University, Tallahassee, Florida 32306, United States*

    Yudan Chen − *Department of Chemistry and Biochemistry, Florida State University, Tallahassee, Florida 32306, United States*

    Pawan K. Ojha − *Department of Chemistry and Biochemistry, Florida State University, Tallahassee, Florida 32306, United States*

    Thilina N. D. D. Gamaralalage − *Department of Chemistry and Biochemistry, Florida State University, Tallahassee, Florida 32306, United States*

    Sawankumar V. Patel − *Department of Chemistry and Biochemistry, Florida State University, Tallahassee, Florida 32306, United States*

    Yongkang Jin − *Department of Chemistry and Biochemistry, Florida State University, Tallahassee, Florida 32306, United States*

    Chen Huang − *Materials Science and Engineering Program, Florida State University, Tallahassee, Florida 32310, United States; Department of Scientific Computing, Florida State University, Tallahassee, Florida 32306, United States;* ⓞ orcid.org/0000-0003-2934-8118

    Tianyi Li − *X-ray Science Division, Argonne National Laboratory, Argonne, Illinois 60439, United States;* ⓞ orcid.org/0000-0002-6234-6096

    Yuzi Liu − *Center for Nanoscale Materials, Argonne National Laboratory, Argonne, Illinois 60439, United States;* ⓞ orcid.org/0000-0002-8733-1683

    Hui Xiong − *Micron School of Materials Science and Engineering, Boise State University, Boise, Idaho 83725, United States;* ⓞ orcid.org/0000-0003-3126-1476

Complete contact information is available at:
https://pubs.acs.org/10.1021/acsenergylett.4c02788

Notes

The authors declare no competing financial interest.

■ ACKNOWLEDGMENTS

■ REFERENCES

(1) Asano, T.; Sakai, A.; Ouchi, S.; Sakaida, M.; Miyazaki, A.; Hasegawa, S. Solid Halide Electrolytes with High Lithium-Ion Conductivity for Application in 4 V Class Bulk-Type All-Solid-State Batteries. *Adv. Mater.* **2018**, *30* (44), 1803075.

(2) Li, X.; Liang, J.; Chen, N.; Luo, J.; Adair, K. R.; Wang, C.; Banis, M. N.; Sham, T.-K.; Zhang, L.; Zhao, S.; Lu, S.; Huang, H.; Li, R.; Sun, X. Water-Mediated Synthesis of a Superionic Halide Solid Electrolyte. *Angew. Chem., Int. Ed. Engl.* **2019**, *58* (46), 16427−16432.

(3) Kraft, M. A.; Culver, S. P.; Calderon, M.; Böcher, F.; Krauskopf, T.; Senyshyn, A.; Dietrich, C.; Zevalkink, A.; Janek, J.; Zeier, W. G. Influence of Lattice Polarizability on the Ionic Conductivity in the Lithium Superionic Argyrodites Li6PS5X (X = Cl, Br, I). *J. Am. Chem. Soc.* **2017**, *139* (31), 10909−10918.

(4) Kamaya, N.; Homma, K.; Yamakawa, Y.; Hirayama, M.; Kanno, R.; Yonemura, M.; Kamiyama, T.; Kato, Y.; Hama, S.; Kawamoto, K.; Mitsui, A. A Lithium Superionic Conductor. *Nat. Mater.* **2011**, *10* (9), 682−686.

(5) Wakamura, K. Correlation between High Ionic Conduction and Anomaly of Dielectric Property. *Solid State Commun.* **1993**, *86* (8), 503−507.

(6) Combs, S. R.; Todd, P. K.; Gorai, P.; Maughan, A. E. Editors' Choice—Review—Designing Defects and Diffusion through Substitutions in Metal Halide Solid Electrolytes. *J. Electrochem. Soc.* **2022**, *169* (4), 040551.

(7) Kim, K.; Park, D.; Jung, H.-G.; Chung, K. Y.; Shim, J. H.; Wood, B. C.; Yu, S. Material Design Strategy for Halide Solid Electrolytes Li3MX6 (X = Cl, Br, and I) for All-Solid-State High-Voltage Li-Ion Batteries. *Chem. Mater.* **2021**, *33* (10), 3669−3677.

(8) Papatheodorou, G. N. Raman Spectroscopic Studies of Yttrium (III) Chloride-Alkali Metal Chloride Melts and of Cs $_2$ NaYCl $_6$ and YCl $_3$ Solid Compounds. *J. Chem. Phys.* **1977**, *66* (7), 2893−2900.

(9) Poudel, T. P.; Deck, M. J.; Wang, P.; Hu, Y.-Y. Transforming Li3PS4 Via Halide Incorporation: A Path to Improved Ionic Conductivity and Stability in All-Solid-State Batteries. *Adv. Funct. Mater.* **2024**, *34* (4), 2309656.

(10) Schlem, R.; Banik, A.; Eckardt, M.; Zobel, M.; Zeier, W. G. Na3-xEr1-xZrxCl6—A Halide-Based Fast Sodium-Ion Conductor with Vacancy-Driven Ionic Transport. *ACS Appl. Energy Mater.* **2020**, *3* (10), 10164−10173.

(11) Deck, M. J.; Chien, P.-H.; Poudel, T. P.; Jin, Y.; Liu, H.; Hu, Y.-Y. Oxygen-Induced Structural Disruption for Improved Li+ Transport and Electrochemical Stability of Li3PS4. *Adv. Energy Mater.* **2024**, *14* (4), 2302785.

(12) Schlem, R.; Banik, A.; Ohno, S.; Suard, E.; Zeier, W. G. Insights into the Lithium Sub-Structure of Superionic Conductors Li3YCl6 and Li3YBr6. *Chem. Mater.* **2021**, *33* (1), 327−337.

(13) Dawson, J. A.; Canepa, P.; Clarke, M. J.; Famprikis, T.; Ghosh, D.; Islam, M. S. Toward Understanding the Different Influences of Grain Boundaries on Ion Transport in Sulfide and Oxide Solid Electrolytes. *Chem. Mater.* **2019**, *31* (14), 5296−5304.

(14) Oh, D. Y.; Choi, Y. E.; Kim, D. H.; Lee, Y.-G.; Kim, B.-S.; Park, J.; Sohn, H.; Jung, Y. S. All-Solid-State Lithium-Ion Batteries with TiS2 Nanosheets and Sulphide Solid Electrolytes. *J. Mater. Chem. A* **2016**, *4* (26), 10329−10335.

(15) Shin, B. R.; Nam, Y. J.; Kim, J. W.; Lee, Y.-G.; Jung, Y. S. Interfacial Architecture for Extra Li+ Storage in All-Solid-State Lithium Batteries. *Sci. Rep.* **2014**, *4* (1), 5572.

(16) Minnmann, P.; Quillman, L.; Burkhardt, S.; Richter, F. H.; Janek, J. Editors' Choice—Quantifying the Impact of Charge Transport Bottlenecks in Composite Cathodes of All-Solid-State Batteries. *J. Electrochem. Soc.* **2021**, *168* (4), 040537.

(17) Bette, S.; Takayama, T.; Duppel, V.; Poulain, A.; Takagi, H.; Dinnebier, R. E. Crystal Structure and Stacking Faults in the Layered Honeycomb, Delafossite-Type Materials Ag3LiIr2O6 and Ag3LiRu2O6. *Dalton Trans.* **2019**, *48* (25), 9250−9259.

(18) Welberry, T. R.; Butler, B. D. Interpretation of Diffuse X-Ray Scattering via Models of Disorder. *J. Appl. Crystallogr.* **1994**, *27* (3), 205−231.

(19) Warren, B. E. X-Ray Diffraction in Random Layer Lattices. *Phys. Rev.* **1941**, *59* (9), 693−698.

(20) Gombotz, M.; Wilkening, H. M. R. Fast Li Ion Dynamics in the Mechanosynthesized Nanostructured Form of the Solid Electrolyte Li3YBr6. *ACS Sustain. Chem. Eng.* **2021**, *9* (2), 743−755.

(21) Bohnsack, A.; Stenzel, F.; Zajonc, A.; Balzer, G.; Wickleder, M. S.; Meyer, G. Ternary Halides of the A3MX6 Type. Part 6. Ternary Chlorides of the Rare-Earth Elements with Lithium, Li3LnCl6 (Ln: Tb-Lu, Y, Sc): Synthesis, Crystal Structures, and Ionic Motion. *Z. Anorg. Allg. Chem.* **1997**, *623* (7), 1067−1073.

(22) Hu, Y.; Fu, J.; Xu, J.; Luo, J.; Zhao, F.; Su, H.; Liu, Y.; Lin, X.; Li, W.; Kim, J. T.; Hao, X.; Yao, X.; Sun, Y.; Ma, J.; Ren, H.; Yang, M.; Huang, Y.; Sun, X. Superionic Amorphous NaTaCl6 Halide Electrolyte for Highly Reversible All-Solid-State Na-Ion Batteries. *Matter* **2024**, *7* (3), 1018−1034.

(23) Bain, A. D. Chemical Exchange in NMR. *Prog. Nucl. Magn. Reson. Spectrosc.* **2003**, *43* (3), 63−103.

(24) Epp, V.; Wilkening, M.Li-Ion Dynamics in Solids as Seen Via Relaxation NMR. In *Handbook of Solid State Batteries*; Dudney, N. J., West, W. C., Nanda, J., Eds.; Materials and Energy, Vol. 6; World Scientific, 2015; pp 133−190, DOI: 10.1142/9789814651905_0005.

(25) Widdifield, C. M.; Chapman, R. P.; Bryce, D. L. Chlorine, Bromine, and Iodine Solid-State NMR Spectroscopy. In *Annual Reports on NMR Spectroscopy*; Elsevier, 2009; Vol. 66, Chapter 5, pp 195−326, .

(26) Bloembergen, N.; Purcell, E. M.; Pound, R. V. Relaxation Effects in Nuclear Magnetic Resonance Absorption. *Phys. Rev.* **1948**, *73* (7), 679−712.

(27) Deck, M. J.; Hu, Y.-Y. Leveraging Local Structural Disorder for Enhanced Ion Transport. *J. Mater. Res.* **2023**, *38* (10), 2631−2644.